Purdue University
Purdue e-Pubs

CTRC Research Publications | Cooling Technologies Research Center

1-1-2000

The Influence of Gravity Levels on the Horizontal Bridgman Crystal Growth of an Alloy

J E. Simpson

S V. Garimella
Purdue Univ, sureshg@purdue.edu

Follow this and additional works at: http://docs.lib.purdue.edu/coolingpubs

Simpson, J E. and Garimella , S V., "The Influence of Gravity Levels on the Horizontal Bridgman Crystal Growth of an Alloy" (2000). *CTRC Research Publications.* Paper 81.
http://docs.lib.purdue.edu/coolingpubs/81

This document has been made available through Purdue e-Pubs, a service of the Purdue University Libraries. Please contact epubs@purdue.edu for additional information.

PERGAMON

International Journal of Heat and Mass Transfer 43 (2000) 1905–1923

International Journal of HEAT and MASS TRANSFER

www.elsevier.com/locate/ijhmt

The influence of gravity levels on the horizontal Bridgman crystal growth of an alloy

James E. Simpson, Suresh V. Garimella*

School of Mechanical Engineering, Purdue University, West Lafayette, IN 47907-1288, USA

Received 23 February 1999; received in revised form 1 September 1999

Abstract

The solidification of a dilute alloy under Bridgman crystal growth conditions in a reduced-gravity environment is investigated. The simulation consists of fully transient calculations of the species concentration, temperature and flow field, as well as conduction in the ampoule. Results are obtained at gravity levels of 1, 10 and 50 μg for a Bi-1.0 at.% Sn alloy to determine the influence of gravity level on thermosolutal convection, and consequently, on the concentration in the solid. A primary convective cell driven by thermal gradients forms in the bulk of the domain, while a secondary convective cell driven by solutal gradients forms near the interface. The magnitude of the velocities in the secondary cell increases with time, causing increasing solute segregation at the interface. For a gravity level of 1 μg, convection-induced radial segregation in the solidified material is minimal and the process is diffusion-controlled. In contrast, at the highest gravity level of 50 μg, very large levels of segregation are observed and the high levels of convective transport in the melt lead to a breakdown in the phenomena normally associated with diffusion-controlled solidification. © 2000 Elsevier Science Ltd. All rights reserved.

1. Introduction

The compositional uniformity (and hence the quality) of crystalline materials synthesized by directional solidification can be profoundly influenced by the transport phenomena which occur in the melt, particularly in the vicinity of the solid–liquid interface, during solidification. The primary transport mechanism controlling crystal quality is natural convection. This convection is driven by density differences caused by both thermal gradients in the material and solute gradients in the layer adjacent to the solid–liquid interface, and so, may exhibit a complex structure. The low-gravity environment of Space offers an opportunity to suppress the strength of this natural convection, so that the process may become *diffusion-controlled*. Hence there is a great deal of interest in the study of the physical processes that take place during directional solidification under low-gravity conditions.

Many simulations of Bridgman crystal growth processes, both under terrestrial and low-gravity conditions, are available in the literature. The majority of these simulations can be classified as *pseudo steady state* models. The key assumption in such models is that a "steady state" mode of alloy solidification exists, i.e. the concentration of the dopant in the solid which forms at the interface is equal to the initial dopant concentration in the liquid [1]. Such models vary in complexity from simple two-dimensional analyses that consider the interface to be flat [2,3] to much more complex for-

* Corresponding author. Tel.: +1-765-494-5621; fax: +1-765-494-0539.

E-mail address: sureshg@ecn.purdue.edu (S.V. Garimella).

0017-9310/00/$ - see front matter © 2000 Elsevier Science Ltd. All rights reserved.
PII: S0017-9310(99)00275-6

Nomenclature

A	apparent heat capacity (Eq. (3))
c_p	specific heat at constant pressure
C	species concentration
D	species diffusion coefficient
E	energy
f	volume fraction
g	mass fraction
$\mathbf{g}$	acceleration due to gravity
Gr	Grashof number, $\mathbf{g}\beta_T(T_H-T_C)H^3/\nu^2$
Gr_s	solutal Grashof number, $\mathbf{g}\beta_c C_0 H^3/\nu^2$
h	ampoule thickness (outside radius−inside radius)
h_0	reference enthalpy of liquid phase, $\Delta H/\rho$
H	ampoule diameter; reference length
k	thermal conductivity
k_p	segregation coefficient
L	length of simulation domain
L_A	translating zone length
Le	Lewis number, α/D
Pr	Prandtl number, ν/α
rhs_{ij}	coefficient matrix in Eq. (11)
RHS_{ij}	coefficient matrix in Eq. (10)
t	time
T	temperature
u, v	velocities in the x, y directions

Greek symbols

β	expansion coefficient
ΔT	temperature difference, T_H-T_C
ΔH	enthalpy of freezing
Γ_{ij}	coefficient matrix in Eq. (10)
Λ_{ij}	coefficient matrix in Eq. (11)
μ	dynamic viscosity
ξ	radial segregation, $(C_{max}-C_{min})/C_{average}$
ρ	density

Subscripts

0	initial condition
C	cold furnace temperature condition
H	hot furnace temperature condition
i, j	located at i, jth finite volume center
I, J	located at I, Jth finite difference mesh point
L	liquid
m	at solidification front
S	solid
w	ampoule wall

Superscripts

$\wedge$	unit vector
$\sim$	vector
$*$	reference quantity
n	time step n

mulations that are able to handle interface curvature and wall conduction [4] and fully three-dimensional simulations [5].

Bridgman growth in Space has previously been modeled by means of a transient, 2D finite-element model [6]. Due to computational difficulties introduced by the small partition coefficient for the system used (Bi–Sn) [5,6], the presence of solute was ignored; as a result, only thermal convection was considered and no quantitative results for solute segregation in the solid were provided. Preliminary scaling arguments on convection levels by de Groh and Nelson [7] imply that solutal convection effects on solute segregation may be significant. However, only recently has it become possible to include solutal convection into numerical simulations involving phase change for transient crystal growth problems.

As a consequence of the low partition coefficient for bismuth doped with tin, a steady-state mode of solidification is never achieved during the Bridgman growth of this material. A solute boundary layer forms in the melt adjacent to the interface and grows with time. The magnitude and structure of solutal convection is determined by this transient solute layer. In turn, the flow velocities influence the solute distribution by convective transport. Since the solute and flow fields are therefore coupled and time-dependent, pseudo steady state models are not appropriate. Instead, fully transient simulations, such as those recently developed by Simpson et al. [8] and Timchenko et al. [9], need to be employed to faithfully model this process.

A key effect during the Bridgman growth process that must be included in simulations is the influence of the ampoule wall. The temperature profile imposed by the furnace is not realized at the inside of the ampoule wall. Heat transfer between the solid, melt ampoule and furnace modifies the temperature profile [2,4]. Longitudinal temperature gradients are generally decreased as a result, while radial temperature gradients may increase or decrease, depending on the combination of melt and ampoule properties. Accurate calculation of convection and the resulting solute segregation can only be achieved if the ampoule is included.

The computational modeling presented in this paper is intended to allow a fundamental examination of the effect of gravity level on horizontal Bridgman crystal

growth experiments performed in Space. Quantitative details of the flow structure, thermal fields and solute redistribution are obtained. This is achieved via a fully transient 2D numerical model, which includes most of the effects of binary alloy solidification, convection driven by both thermal and solutal gradients, distinct thermal properties in the solid and liquid phases, and the effects of interface curvature. Conduction through the ampoule wall is considered. For the purposes of our model, we assume that the liquid/solid interface remains distinct like that for a pure material. This is a valid assumption for the dilute alloy, very slow growth rate, and imposed temperature gradients considered in this study. It will be seen that at very low gravity levels (1 μg), the process is diffusion-controlled, and convection-induced radial and longitudinal segregation is slight. At a gravity level of 10 μg, the process is perturbed from the diffusion-controlled state and discernible levels of segregation occur. As gravity is increased further, the process breaks down and becomes convection-controlled.

2. The mathematical model

The problem under consideration is the directional solidification of a binary alloy by the Bridgman process, as shown schematically in Fig. 1. The gravity vector is perpendicular to the furnace axis (horizontal Bridgman growth configuration). The melt region is considered to be a viscous Newtonian fluid subject to thermosolutal convection. Thermophysical properties are considered as constant but distinct for the solid and liquid phases. Density variations are considered to be subject to the Boussinesq approximation. The governing equations for the velocity field in terms of vorticity and vector potential equations, as well as the boundary conditions employed, are discussed in detail in Simpson and Garimella [10,11] and are not repeated here. In the nondimensionalizations used, the ampoule inside diameter H is selected to be the reference length. The characteristic time and velocity become t^* ($= H^2/\alpha$) and v^* ($= H/t^* = \alpha/H$).

The governing equation for the conservation of energy (from [12]) is

$$A(T,C)\frac{\partial T}{\partial t} + \rho c_{\mathrm{pL}}\tilde{\nabla}(\tilde{u}T) = \tilde{\nabla}(k\tilde{\nabla}T) + B(T,C) \qquad (1)$$

It will be seen that effective heat capacity A and source term B may be specified in this way for calculating phase-change. An initial temperature equal to T_{H} is applied throughout the flow field. The temperatures at

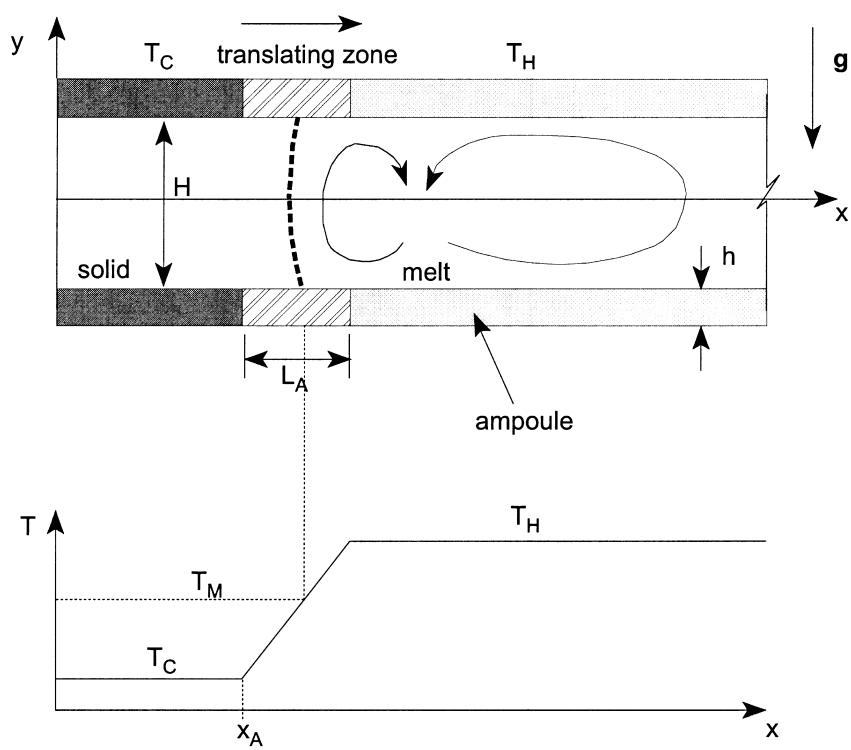

Fig. 1. Schematic of the Bridgman crystal growth process and furnace temperature profile.

the $x = 0$ and $x = L$ walls are set to be T_H and T_C, respectively.

The thermal boundary conditions along $y = \pm(H/2 + h)$ required for the Bridgman process are a function of time, and are shown schematically in Fig. 1. There is a translating zone (considered an "adiabatic" zone if the temperature profile is unknown) between the hot and cold regions of the furnace, in which the temperature linearly increases from the cold furnace temperature to the hot furnace temperature. The melting temperature of the material falls somewhere within this zone, which translates with time at a constant x-velocity, known as the *translation velocity*, u_t. This is what facilitates the directional growth of the crystal. Defining the x location where the translating zone meets the cold furnace temperature zone to be at $x_A(t)$, the boundary condition for temperature may be expressed as

$$\text{at } y = \pm\left(\frac{H}{2} + h\right): T = \begin{cases} T_C, & \text{for } x < x_A(t) \\ T_C + \Delta T \dfrac{x - x_A(t)}{L_A}, & \text{for } x_A(t) \le x \le [x_A(t) + L_A] \\ T_H, & \text{for } x_A(t) < x \end{cases} \tag{2}$$

In principle, the solution of the energy Eq. (1) coupled with the solution of the vorticity-vector potential equations would yield the temperature and velocity distribution throughout the simulation domain. However, the problem of modeling the physics of the propagation of the solidification front and determining its location remains to be addressed. We choose to do this by employing the phase-transformation model of Zeng and Faghri [12]. In their model, apparent heat capacity A and source term B are given as

$$A(T, C) = \rho c_p + a(T, C)\frac{\partial f_L}{\partial T}$$

$$B(T, C) = -\tilde{\nabla}(\rho h_0 \tilde{u}) + \tilde{\nabla}[\rho f_S(h_0 + (c_{pL} - c_{pS})T)\tilde{u}_s] - a(T, C)\frac{\partial f_L}{\partial C}\frac{\partial C}{\partial t}$$

$$a(T, C) = \rho\left[(c_{pL} - c_{pS})T + \frac{(\rho_L - \rho_S)c_p T + \rho_L h_0}{\rho_L - f_L(\rho_L - \rho_S)}\right]$$

$$c_p = c_{pL} f_L + c_{pS} f_S$$

$$\rho = \rho_S g_S + \rho_L g_L \tag{3a}$$

For the present study, concentration-dependence on temperature is neglected, the density of each phase is assumed to be equal, and there is no dispersion of solid phase moving in the liquid. After these assumptions are made, the full expressions for A and B (Eq. (3a)) simplify to become

$$A(T) = \rho(c_{pL} f_L + c_{pS} f_S) + a(T)\frac{\partial f_L}{\partial T}$$

$$B(T) = 0$$

$$a(T) = \rho[(c_{pL} - c_{pS})T + h_0] \tag{3b}$$

Since source term B has become zero, this scheme may be classified as an *apparent heat capacity method* [6,13].

The equation for conservation of solute throughout the computational domain is

$$\frac{\partial C_L}{\partial t} + \tilde{\nabla}(\tilde{u} C_L) = D\nabla^2 C_L + S(T, C_L) \tag{4}$$

This equation is analogous to the energy equation. We impose an initial solute concentration throughout the solution domain. At the boundaries no solute may exit the solution domain. Thus,

$$t = 0 \quad C_L = C_0$$

$$x = 0, L \quad \partial C_L/\partial x = 0$$

$$y = 0, H \quad \partial C_L/\partial y = 0 \tag{5}$$

Again, in principle, solution of Eq. (4) along with energy Eq. (1) and the vorticity-vector potential equations all subject to the relevant boundary and initial conditions would yield the solute, temperature and velocity values throughout the solution domain. However, the more general problem involving phase change demands that the thermodynamics of solute redistribution be addressed. Source term S is the mechanism by which solute rejection into the melt region at the advancing solid–liquid interface is accounted for. Following the work of Voller et al. [14] and Swaminathan and Voller [15] term S becomes

$$S(T, C) = \frac{\partial(f_L C_L)}{\partial t} + k_p C_L \frac{\partial f_S}{\partial t} \tag{6}$$

The following assumptions have been employed in the development of Eq. (6):

1. the densities of the liquid and solid phases are constant and equal;
2. there is no diffusion in the solid (except in the cells that contain the interface, in which the equilibrium lever rule is assumed); the concentration at which

the solute first solidifies is the concentration at which that portion of solid remains for all time t.

The important parameters are the partition or distribution coefficient, k_p, and the slope of the liquidus line, m. For the purposes of our model, we assume that $T_L \approx T_S \approx T_M$ at the interface for all concentrations encountered; thus, there is no effect of concentration on melting temperature and the liquid/solid interface remains distinct like that for a pure material. The significant result of this assumption is that the energy equation (Eq. (1)) is decoupled from the concentration equation and is the only mechanism necessary to determine the location of the solidification front.

The mathematical formulation for the directional solidification of a binary alloy subject to thermosolutal convection has now been fully specified. The next step is to formulate an appropriate solution scheme so that results may be obtained.

3. The numerical scheme

The computational domain is primarily discretized using regularly spaced finite difference mesh points. Superimposed on this grid are finite volumes which are used for the solution of the energy and species concentration equations (Fig. 2). Vorticity, velocity and stream function are calculated at the finite difference mesh points. Temperature and solute concentration are evaluated at the finite volume centers as a result of the solution of Eqs. (1) and (4). The finite volume centers are staggered with respect to the finite difference mesh point locations in order to obtain the most accurate interpolated values for velocity at the finite volume faces.

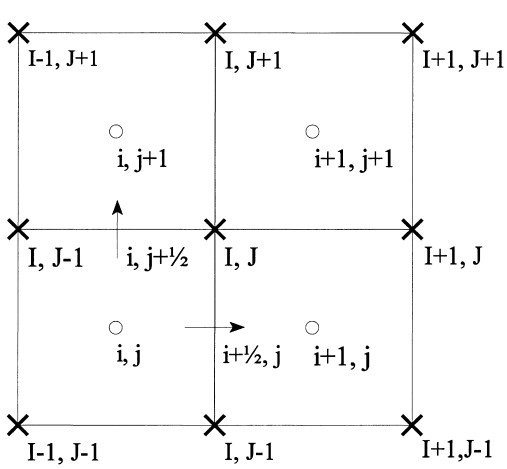

Fig. 2. Arrangement of finite volume centers and finite difference mesh points.

The details of the solution scheme for the vorticity transport and stream function equations, including the application of boundary conditions at the arbitrarily-oriented solid–liquid interface, are furnished in Simpson and Garimella [10,11] and are not repeated here.

The discretized energy equation is shown in Appendix A. The key to facilitating phase-change in this formulation lies in specifying the change in liquid volume fraction with temperature. In principle, the relationship between liquid volume fraction and temperature for a material with a distinct melting temperature T_m is

$$f_L = \begin{cases} 0, & \text{if } T_{i,j} \le T_m \\ 1, & \text{if } T_{i,j} > T_m \end{cases} \tag{7}$$

In practice, numerical algorithms are unable to handle the point discontinuity; the relationship between liquid fraction and temperature must be linearly smoothed at T_m [6,13]. This results in the relations

$$f_L = \begin{cases} 0, & \text{if } T_{i,j} < (T_m - \varepsilon) \\ \dfrac{T - T_m + \varepsilon}{2\varepsilon}, & \text{if } (T_m - \varepsilon) \le T_{i,j} \le (T_m + \varepsilon) \\ 1, & \text{if } T_{i,j} > (T_m + \varepsilon) \end{cases} \tag{8}$$

and

$$\left.\frac{\partial f_L}{\partial T}\right|_{i,j} = \begin{cases} 0, & \text{if } T_{i,j} < (T_m - \varepsilon) \\ \dfrac{1}{2\varepsilon}, & \text{if } (T_m - \varepsilon) \le T_{i,j} \le (T_m + \varepsilon) \\ 0, & \text{if } T_{i,j} > (T_m + \varepsilon) \end{cases} \tag{9}$$

Fidelity of the solution scheme is ensured if temperature increment 2ε is kept small. This is achieved by selecting 2ε to be equal to the temperature change that a single cell undergoes in one time step due to the applied transient temperature gradient. Values lower than this result in oscillations in the solution or a lowering of the latent heat released at the interface, while higher values result in the latent heat being released at a range of locations away from the interface. The system of equations formed from the numerical formulation is advanced forward in time using Gauss–Seidel iteration with successive over relaxation which may be written as

$$[A_{i,j}^p + \Gamma_{i,j}^p]T_{i,j}^{p+1} = \mathrm{RHS}_{i,j}^p \tag{10}$$

in which p denotes the inner iteration number, and the values at time step n are used as the first approximation. The RHS is fully explicit at iteration p. Iterations proceed until convergence, at which time the new values at time step $(n + 1)$ for temperature and enthalpy are declared to be those found at conver-

gence. Convergence is assessed in the usual manner with a tolerance of 10^{-6} [16,17].

The discrete form of the concentration Eq. (4) is given in Appendix B. The solution of this equation is attained via Gauss–Seidel iteration in a manner analogous to the energy equation, i.e.,

$$[1+\Lambda_{ij}^{p}]C_{\mathrm{L},\,ij}^{p+1} = \mathrm{rhs}_{ij}^{p} \tag{11}$$

Since diffusion in the solid is negligible, the solute concentration in the solid portion of a node may be recovered by employing the relation

$$C_{\mathrm{S}}^{n+1} = \frac{C_{\mathrm{S}}^{n} f_{\mathrm{S}}^{n} + k_{\mathrm{p}} C_{\mathrm{L}}^{n}(f_{\mathrm{L}}^{n+1} - f_{\mathrm{L}}^{n})}{f_{\mathrm{S}}^{n+1}} \tag{12}$$

The solution scheme for solidification in a two-dimensional cavity subject to thermosolutal convection has now been fully specified.

4. Results and discussion

Simulations for the Bridgman crystal growth of a Bi-1.0 at.% Sn alloy (0.8185 vol.% Sn) at gravity levels of 1, 10 and 50 μg were performed (yielding Grashof numbers of Gr = 11.36, 113.6, 568.0 and solutal Grashof numbers of $Gr_{\mathrm{S}} = 0.4262$, 4.262, 21.31, respectively). Thermophysical properties from [3] were used. The property values are provided in Table 1. The cold and hot furnace temperatures were $T_{\mathrm{C}} = 50°\mathrm{C}$ and $T_{\mathrm{H}} = 700°\mathrm{C}$, respectively. Liquid properties were used as the reference properties in the nondimensionalization. The dimensions used to define the domain were L = 75 mm and H = 6 mm. The ampoule wall thickness, h, was 2 mm. The length of the insulated translating zone was $L_{\mathrm{A}} = 25$ mm, with a translation velocity of $u_{\mathrm{t}} = 3.38$ μm/s.

In order to start the crystal growth simulations, the following procedure was carried out in each simulation. The initial position of the translating zone was flush with the x = 0 wall. This zone is immobilized for the first 3000 time steps. During this time, the velocity and concentration field solution schemes are switched off while solid rapidly chills in the portion of the translating zone which is lower than the melting temperature. This new state is then taken to be at time t = 0. After this, simulations proceed with the entire solution scheme enabled and the insulated zone moving at the translation velocity u_{t}.

4.1. Overview of grid independence tests

A grid independence study was undertaken to determine the appropriate spatial and temporal discretization scheme to be used. This study involved examining the solution fields from a test matrix of simulations performed using four different discretization schemes. The thermal, solutal and velocity fields were examined

Table 1
Thermophysical properties[a]

Property	Units	Value
Reference density, ρ_0	kg/m^3	10,070
Thermal conductivity of the solid, k_{S}	W/m K	6.872
Thermal conductivity of the liquid, k_{L}	W/m K	14.66
Specific heat of the solid, c_{pS}	J/kg K	132.6
Specific heat of the liquid, c_{pL}	J/kg K	135.3
Enthalpy of freezing, ΔH	kJ/kg	52.3
Viscosity of the liquid, μ	Ns/m	1.240×10^{-3}
Melting temperature, T_{m}	°C	271.3
Thermal expansion coefficient, β_{T}	K^{-1}	-1.25×10^{-4}
Thermal conductivity of the (fused silica) ampoule, k_{w}	W/m K	2.10
Density of the (fused silica) ampoule, ρ_{w}	kg/m^3	2020
Specific heat of the (fused silica) ampoule, c_{pw}	J/kg K	1066.8
Partition (or segregation) coefficient, k_{p}	–	0.029
Diffusivity of liquid Sn in liquid Bi, D	m^2/s	3.50×10^{-9}
Solutal expansion coefficient, β_{C}	(vol.%)$^{-1}$	−0.305
Prandtl number, Pr	–	0.01144
Lewis number, Le	–	3074

[a] The properties (except the solutal diffusion coefficient D) for solid and liquid bismuth were evaluated at the mean solid and the mean liquid temperatures of 160.7 and 485.7°C, respectively. The solutal diffusion coefficient was evaluated at a position halfway into a typical solute boundary layer, since solute diffusion occurs mainly in this region. The reference density was considered to be equal for both phases.

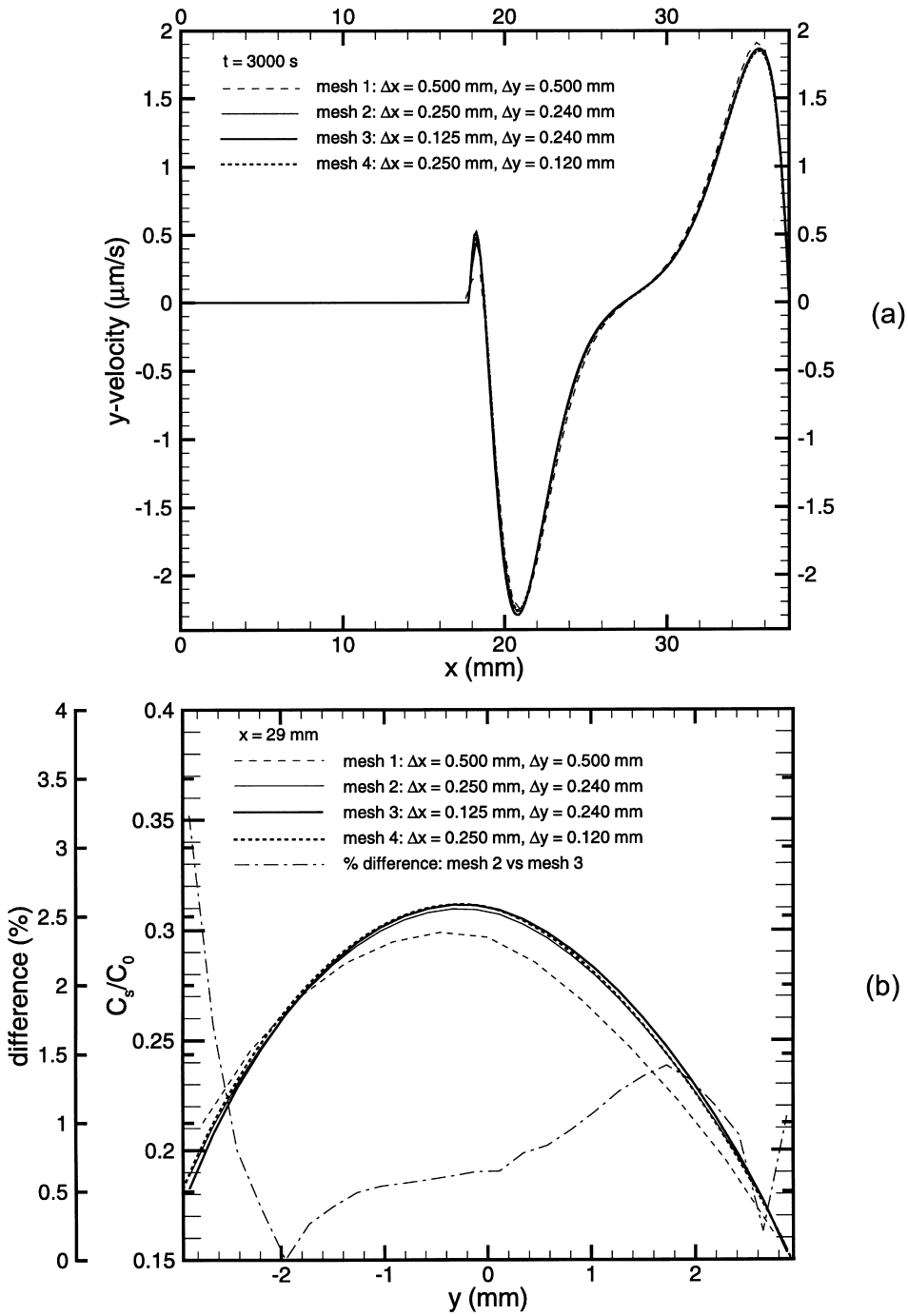

Fig. 3. Results from grid-independence study: (a) trace of y-velocities along $y = 0$; (b) radial solute concentration profiles in the solid at $x = 29$ mm. Mesh 2 is seen to be adequate for the simulations.

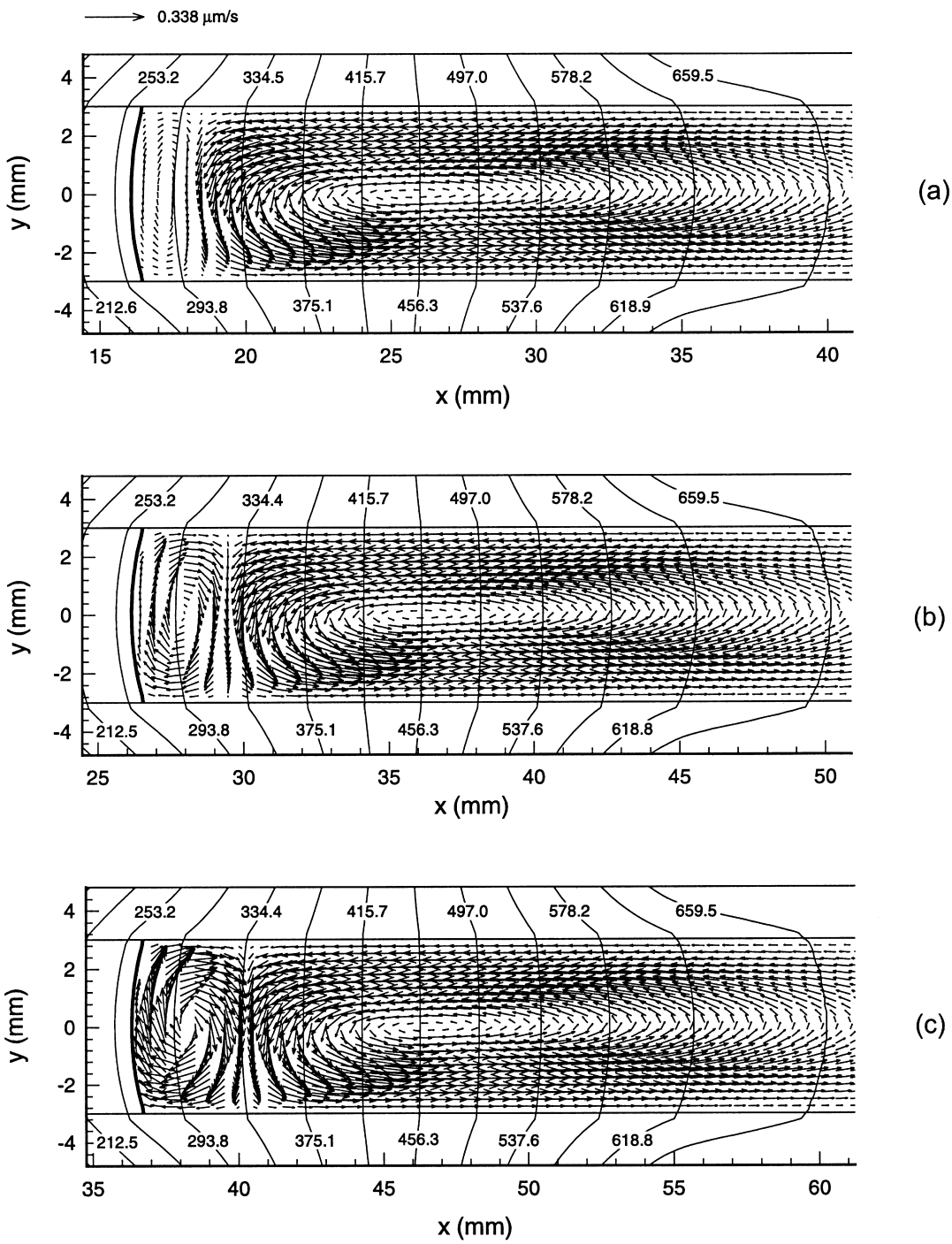

Fig. 4. Velocity vectors and isotherms for horizontal Bridgman growth with $g = 1$ μg at (a) 3000 (b) 6000 and (c) 9000 s. The thick solid line indicates the location of the solid–liquid interface. Velocity vectors are shown at every other location in the x-direction.

after a time of $t = 3000$ s. In order to conserve CPU time, the presence of the ampoule was neglected and the length of the computational domain in the x-direction was cut down to 37.5 mm for these test runs. This was feasible since the crystal does not become long enough to cause the flow field to significantly interact with the end of the domain at $t = 3000$ s. The gravity level was set at $g = 10$ μg. The mesh sizes investigated were:

- mesh 1 — a coarse mesh, $\Delta x = 0.5$ mm, $\Delta y = 0.5$ mm and $\Delta t = 0.5807$ s;
- mesh 2 — the preferred mesh, $\Delta x = 0.25$ mm, $\Delta y = 0.24$ mm and $\Delta t = 0.1338$ s;
- mesh 3 — an x-refined mesh, $\Delta x = 0.125$ mm, $\Delta y = 0.24$ mm and $\Delta t = 0.03630$ s;
- mesh 4 — a y-refined mesh, $\Delta x = 0.25$ mm, $\Delta y = 0.12$ mm and $\Delta t = 0.03345$ s.

The results are briefly discussed here. The thermal field results were almost identical for all four schemes. A trace of y-velocities after $t = 3000$ s is shown in Fig. 3(a). At this time, the maximum magnitudes of y-velocity predicted by the four meshes are 2.238, 2.265, 2.292 and 2.256 μm/s for each respective mesh. The differences between the values predicted from mesh 1 and mesh 3 are less than 10% over the majority of the domain; this difference reduces to less than 3% (compared to mesh 3) when mesh 2 is used. These differences are typical of those found at other times, indicating that discrepancies are not accumulating with time. Particular attention was paid to the concentration values in the solidified material. The concentrations in the solid are completely dependent on the solutal, thermal and flow fields in the melt, and thus are very sensitive to any changes in these fields. Concentration traces across the solidified material at $x = 29$ mm (a location just behind the interface at $t = 3000$ s) are shown in Fig. 3(b). As can be readily observed from this plot, the values found using mesh 1 exhibit serious discrepancies when compared to the finer meshes, while those obtained using mesh 2 are close to those found using the finer meshes 3 and 4. A plot of the percentage difference between the results found using meshes 2 and 3 is also superimposed on Fig. 3(b). The maximum discrepancy is only 3.2%, while the majority of the values are smaller than 1%. Analysis of these results makes it clear that the algorithm will converge to an exact solution, and that mesh 2 is fine enough to obtain meaningful results.

4.2. $g = 1$ μg

Velocity vectors and isotherms after 3000, 6000 and 9000 s for this gravity level are shown in Fig. 4. Isotherms are shown in the ampoule wall as well as in the liquid and solid regions. The velocity vectors in Fig. 4(a) indicate a primary convective cell rotating in a counter-clockwise manner in the translating zone, along with a weak secondary, clockwise convective cell driven by solute gradients adjacent to the interface (the thick line at $x \approx 16$ mm represents the solid–liquid interface). This two-cell convective motion is in contrast to the single-cell convective motions observed for pure materials and more dilute alloys [18]. For clarity, velocity vectors are plotted on every second mesh point in the x-direction in this figure. Solute rejection at the interface leading to the formation of a solute boundary layer adjacent to the interface is responsible for the formation of the secondary cell.

The other main feature of this plot is the isotherms throughout the solution domain. On the outside edge of the ampoule, the (imposed) temperature profile is a linear ramp function within the translating zone, as witnessed by the regularly spaced isotherms on the outer edge. In the ampoule region, the isotherms are dramatically distorted. Since the ampoule material (fused silica) has a low thermal conductivity, the thermal field on the inside of the ampoule wall differs from that imposed on the outside. The isotherms and the interface appear to be symmetric about the centerline ($y = 0$) and thus have not been influenced by convective transport in the melt. Note that the solid–liquid interface, which is an isotherm, is discernibly curved such that the solid is concave. The total deflection of the interface is about 0.5 mm which compares to a value of ~0.46 mm found in [6]. This curvature is primarily a result of the difference in thermophysical properties for the solid and liquid phases. Translation of the thermal boundary condition also contributes to this effect. Maximum velocity magnitudes and their locations for this case are provided in Table 2. These values show that velocities in the thermally driven convective cell are much higher than those found in the secondary cell at this time.

At a later time (6000 s), the front is at $x \approx 26$ mm, as shown in Fig. 4(b). The secondary convective cell has increased in size and strength as solute — the driving force for this cell — continues to build up at the interface. Later in the growth process (9000 s, Fig. 4(c)), the front has advanced to $x \approx 36$ mm, and the secondary convective cell is almost as strong as the primary cell (refer to Table 2). However, since the magnitude of the velocities in the domain in all cases is small (< 1 μm/s), we anticipate that there would be only a minimal impact of convection on solute segregation. The curvature of the interface is also seen to remain unchanged at these later times.

Traces of solute concentration across the height of the solidified alloy in the domain are shown in Fig. 5. Three different x-locations (16.18, 26.30, 36.41 mm) are considered; these locations correspond to the location of the interface at $y = 0$ at times of 3000, 6000

Table 2
Maximum velocity magnitudes (and locations) in the primary and secondary cells determined at each gravity level[a]

$\lvert U \rvert = (u^2 + v^2)^{1/2}$	3000 s	6000 s	9000 s
1 μg			
Primary cell (x, y)	0.3448 (25.5, ±1.80)	0.3433 (36.0, ±1.80)	0.3426 (46.3, ±1.80)
Secondary cell (x, y)	0.05860 (16.5, 0.120)	0.1794 (27.0, 0.120)	0.3125 (37.0, 0.120)
4 10 μg			
Primary cell (x, y)	3.444 (25.5, ±1.80)	3.429 (36.0, ±1.80)	3.411 (46.6, ±1.80)
Secondary cell (x, y)	0.5745 (16.5, 0.120)	1.754 (27.0, 0.600)	2.878 (37.0, 0.360)
50 μg			
Primary cell (x, y)	17.22 (25.5, ±1.80)	17.21 (35.7, ±1.80)	17.04 (46.6, ±1.80)
Secondary cell (x, y)	1.183 (16.5, −0.120)	5.224 (27.0, 1.08)	7.774 (38.7, 2.28)

[a] Velocity values are in μm/s and (x, y) are in mm.

and 9000 s, respectively. To aid in visualizing the influence of convection, results for a simulation involving diffusion only (no convection) are superimposed on this plot (dotted lines). Note that these pure diffusion results indicate that significant radial segregation arises due to interface curvature [4,5,19] such that the values for solute concentration at the centerline are larger than those at the edges. The level of curvature-induced

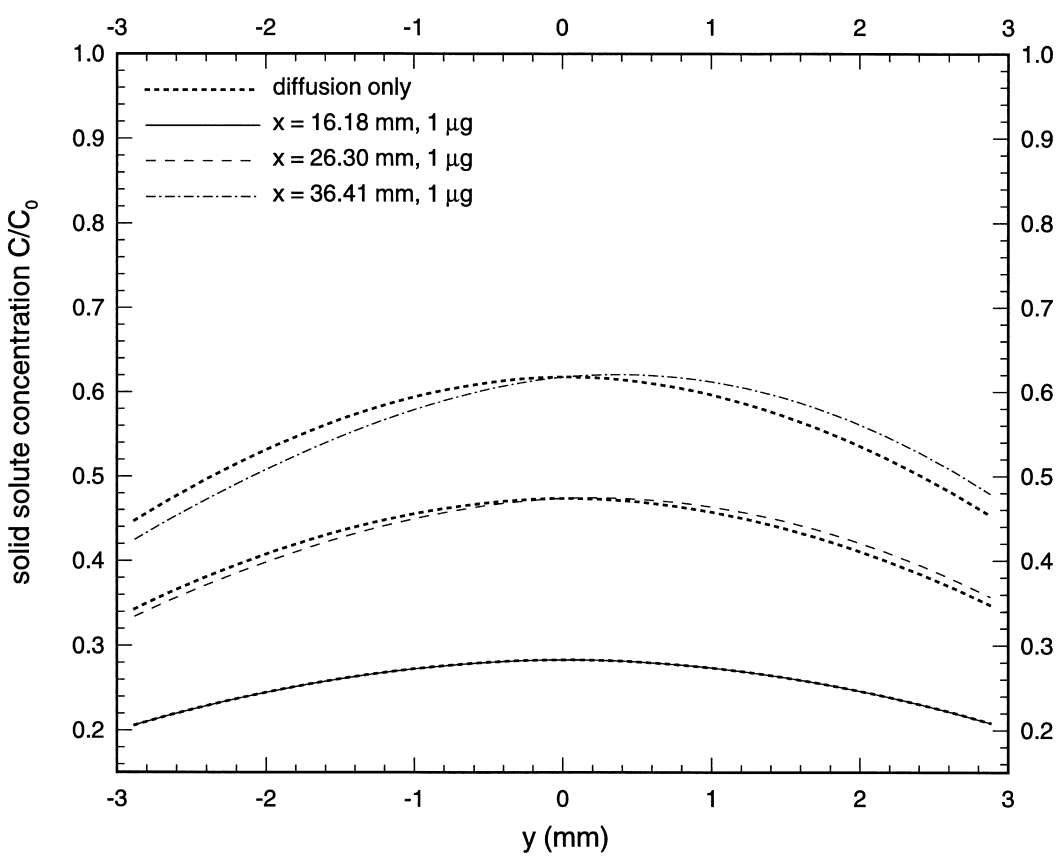

Fig. 5. Traces of solute concentration across the solidified material at various x-locations for $g = 1$ μg. The dotted lines correspond to diffusion-only (no convection) results.

Table 3
Concentration values and radial segregation levels in the solidified crystal at various x locations

Quantity	x = 16.18 mm	x = 26.30 mm	x = 36.41 mm
0 μg (diffusion only case)			
C_{av}/C_0	0.2564	0.4276	0.5576
C_{max}/C_0	0.2834 (y = 0)	0.4737 (y = 0)	0.6179 (y = 0)
ξ (%)	29.7	30.0	30.0
1 μg			
C_{av}/C_0	0.2564	0.4279	0.5582
C_{max}/C_0	0.2833 (y = 0.059)	0.4745 (y = 0.18)	0.6208 (y = 0.41)
ξ (%)	30.0	32.8	35.1
10 μg			
C_{av}/C_0	0.2545	0.4228	0.5482
C_{max}/C_0	0.2812 (y = 0.059)	0.5063 (y = 1.6)	0.7509 (y = 2.2)
ξ (%)	29.5	55.9	83.9
50 μg			
C_{av}/C_0	0.2071	0.3410	0.4373
C_{max}/C_0	0.2337 (y = −0.088)	0.5171 (y = 2.5)	0.7922 (y = 2.6)
ξ (%)	42.5	95.7	134

radial segregation for the pure diffusion case remains almost constant for each x-location (refer to Table 3). The inclusion of convection into the calculations causes the following effects. The formation and growth of the secondary cell causes additional, convection-based segregation to occur such that concentration values near the top of the domain (positive y) are higher than those at the bottom. For the trace at x = 16.18 mm, the concentration values are close to the values predicted from the pure diffusion analysis, and the maximum is at the centerline (y = 0). At higher values of x (t > 3000 s) this maximum is shifted slightly from the centerline to a more positive y value. The traces at x = 26.30 and 36.41 mm indicate levels of radial segregation slightly increasing over the values found for the pure diffusion case, and a slight shift away from the centerline in the location of maximum concentration (Table 3). This small effect is due to increasing levels of solutal convection with time (refer to Fig. 4 and Table 2).

Fig. 6 is a plot of longitudinal solute traces in both the melt and the solidified crystal, at domain heights of y = −2.88, 0 and 2.88 mm at times of 3000, 6000 and 9000 s. There is significant solute buildup, with the solute boundary layer clearly growing with time (refer to Table 4 for interface concentrations). The solute profiles are similar in nature to the expected traces for a diffusion-only case; convection has had a minimal influence on the solute profiles. Near the interface, the values for solute in the liquid are slightly higher for the y = 2.88 mm trace than that for y = −2.88 mm. Further from the interface, but still within the solute boundary layer, this effect diminishes. This is due to the interaction of the two convective cells. Close to the interface, the secondary cell circulates solute-rich material within the boundary layer, acting to accumulate solute-rich material in this region. Note that concentration values at the interface of the magnitudes indicated in Table 4 would be sufficient to

Table 4
Liquid concentration values at the interface (C^*/C_0) at different domain heights

Domain height	3000 s	6000 s	9000 s
0 μg (diffusion only case)			
y = −2.88 mm	7.38	12.0	15.6
y = 0	9.78	16.3	21.3
y = 2.88 mm	7.38	12.0	15.6
1 μg			
y = −2.88 mm	7.37	11.7	14.8
y = 0	9.78	16.3	21.3
y = 2.88 mm	7.47	12.5	16.7
10 μg			
y = −2.88 mm	7.30	9.36	10.1
y = 0	9.70	15.6	19.2
y = 2.88 mm	7.47	15.8	24.6
50 μg			
y = −2.88 mm	6.74	6.58	7.14
y = 0	7.85	10.9	12.9
y = 2.88 mm	5.40	17.9	27.4

lower the melting temperature of the alloy by a significant amount [18]. This implies that the constant melting temperature assumption is not suitable. The likely effect of the inclusion of a concentration-dependent melting temperature would be to cause the interface to be thicker near the bottom of the domain. This effect may alter the concentration and velocity fields and will be addressed in future work.

4.3. $g = 10$ μg

Velocity vectors and isotherms for this case are similar in nature (but larger in magnitude) to those shown for the g = 1 μg case (Fig. 4) and are not shown. Values for maximum velocities in the primary and secondary cells are provided in Table 2. Traces of solute concentration across the height of the solidified alloy, along with pure diffusion results, are shown in Fig. 7 and Table 3. The increased levels of convection have caused the following effects. For the trace at x = 16.18 mm, the concentration values are close to the values predicted from the pure diffusion analysis. This serendipitous result is a consequence of segregation arising from the influence of the secondary cell balancing the reverse segregation caused by the thermally driven cell when solidification has proceeded to this location. At lower values of x (t < 3000 s), segregation is such that the maximum value occurs at y < 0 while at higher values of x (t > 3000 s) this maximum is shifted noticeably to a more positive y value. The traces at x = 26.30 and 36.41 mm show that increasing solutal convection leads to increasing radial segregation. This behavior is different from the case shown in Fig. 5, where the lower levels in convection resulted in only slight levels of convection-induced segregation.

Fig. 8 is a plot of longitudinal solute traces at domain heights of $y = -2.88$, 0 and 2.88 mm for the g = 10 μg at times of 3000, 6000 and 9000 s. Numerical values for interface concentrations are provided in Table 4. As for the g = 1 μg case (shown in Fig. 6) there is significant solute buildup. Note, however, that the solute boundary layers are discernibly different at

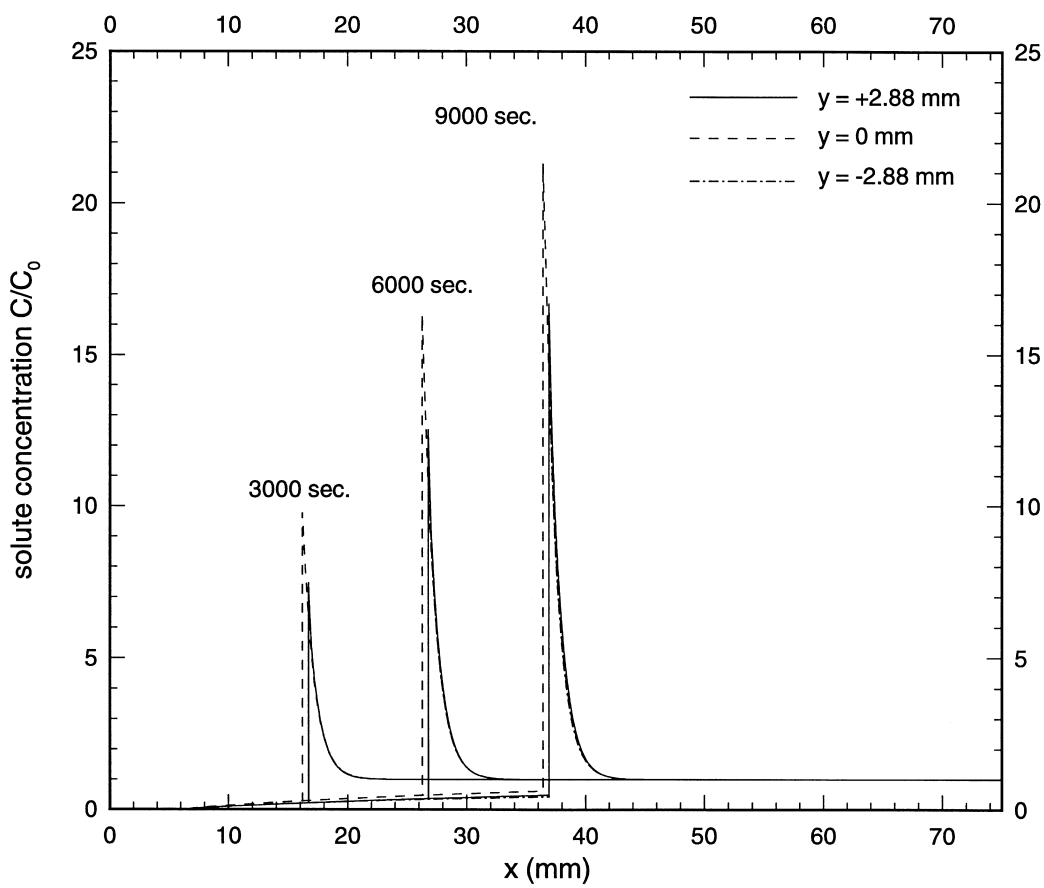

Fig. 6. Longitudinal solute concentration traces at three different y-locations for g = 1 μg.

the three y-locations. Near the interface, the values for solute in the liquid are higher for the y = 2.88 mm trace than for $y = -2.88$ mm. Further from the interface, but still within the solute boundary layer, concentration increases with decreasing y. This is due to the interaction of the two convective cells. Close to the interface, the secondary cell circulates solute-rich material within the boundary layer, acting to accumulate solute-rich material in this region. Further from the interface (see Fig. 4 for example), the primary convective cell influences the solute distribution, sweeping solute from the bottom of the domain into the bulk and thickening the solute boundary layer in this region. In general, the solute boundary layers are more compact near the interface than for the g = 1 μg case at each corresponding time.

For a gravity level of g = 10 μg, thermosolutal convection plays a much larger role than for the g = 1 μg case, as can be seen in the concentration profiles discussed above. As growth proceeds, the level of solutal convection grows, with a corresponding increase in radial segregation. The maximum concentration increases much more rapidly than the minimum value.

4.4. $g = 50$ μg

Velocity vectors and isotherms after 3000, 6000 and 9000 s for this gravity level are shown in Fig. 9. Numerical values for various velocities are given in Table 2. Note the much larger scale of velocity on this plot compared to that used in Fig. 4; the velocities are much larger due to the increased level of gravity. Also note that vectors are again shown at every other mesh point in the x-direction for clarity. After 3000 s (Fig. 9a), there is a weak, solute-driven secondary cell near the interface which counter-acts a primary, thermally-driven convective cell. Note the small x-direction span of the secondary cell. After 6000 s, increasing solute rejection has led to the formation of a much larger (and stronger) secondary cell. This secondary cell is significantly different in nature to those observed for the lower gravity levels after the same amount of time

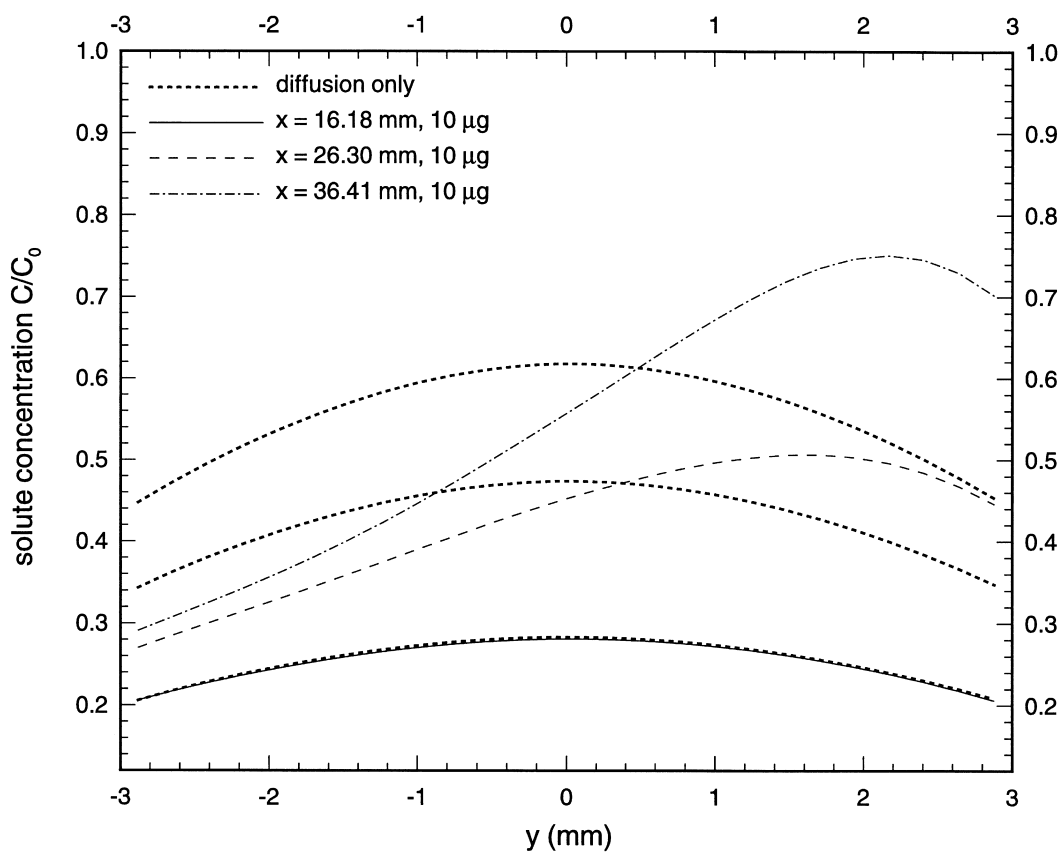

Fig. 7. Traces of solute concentration across the solidified material at various x-locations for g = 10 μg. The dotted lines correspond to diffusion-only (no convection) results.

has elapsed (6000 s, refer to Fig. 4b). In contrast to the lower gravity cases, the center of the cell has moved away from the centerline ($y = 0$) and instead lies at $y \approx 1.2$ mm. The secondary cell is larger and also increases in thickness with increasing y; it is much thicker in the $y > 0$ portion of the domain. These effects are due to increased levels of convection-induced radial and longitudinal segregation and will be expanded upon later in this section. After 9000 s (Fig. 9c), the secondary cell has increased in size and magnitude. The center of the cell remains at $y \approx 1.2$ mm. At this time the magnitudes of the velocities near the interface have become quite large (refer to Table 2).

Fig. 10 is a plot of solute concentration across the height of the solidified alloy, along with pure-diffusion results. Once again, numerical values are provided in Table 3. As anticipated from the flow structure indicated in Fig. 9, the high levels of convection have resulted in greatly increased levels of radial segregation. Large velocities in the positive y direction near the interface act to sweep solute such that the sample is solute-rich as y increases. For all three traces shown, the segregation pattern for $g = 50$ μg is significantly different from the diffusion-only result. This differs from the cases where convection levels are lower (Figs. 5 and 7) where the traces retained some of the characteristics of the diffusion-only result. For the $x = 16.18$ mm case, the maximum value in concentration occurs at $y < 0$; at this time the secondary convective cell driven by solutal gradients (refer to Fig. 9a) has not become strong enough to counter-act the segregation caused by the thermal cell up to this point. For the other traces ($x = 26.30$, 36.41 mm), the increasing strength of the secondary cell causes increasing levels of segregation and a shift in the location of the maximum value to the y > 0 region. Also note that the average value of concentration across the domain is significantly lower for this case than for the diffusion-only result. This is a further indication of a move away from diffusion-dominated conditions and will be expanded upon later.

Fig. 11 is a plot of longitudinal solute traces in the

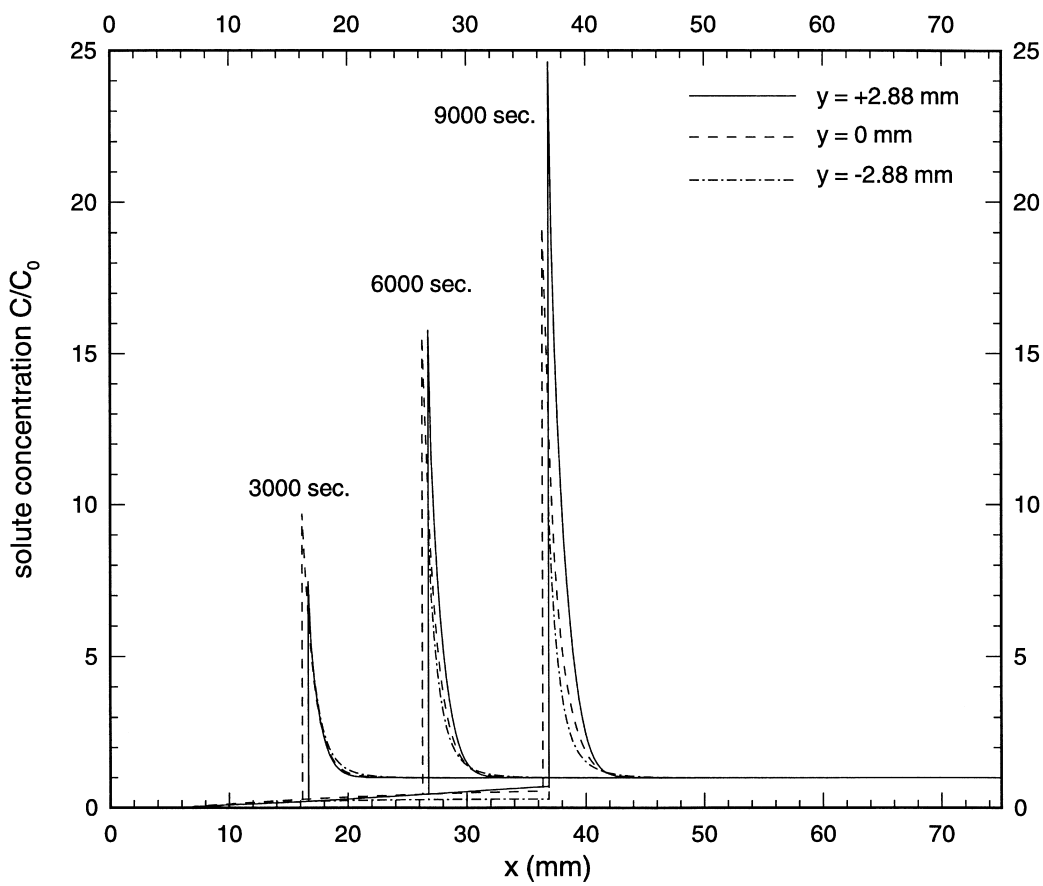

Fig. 8. Longitudinal solute concentration traces at three different y-locations for $g = 10$ μg.

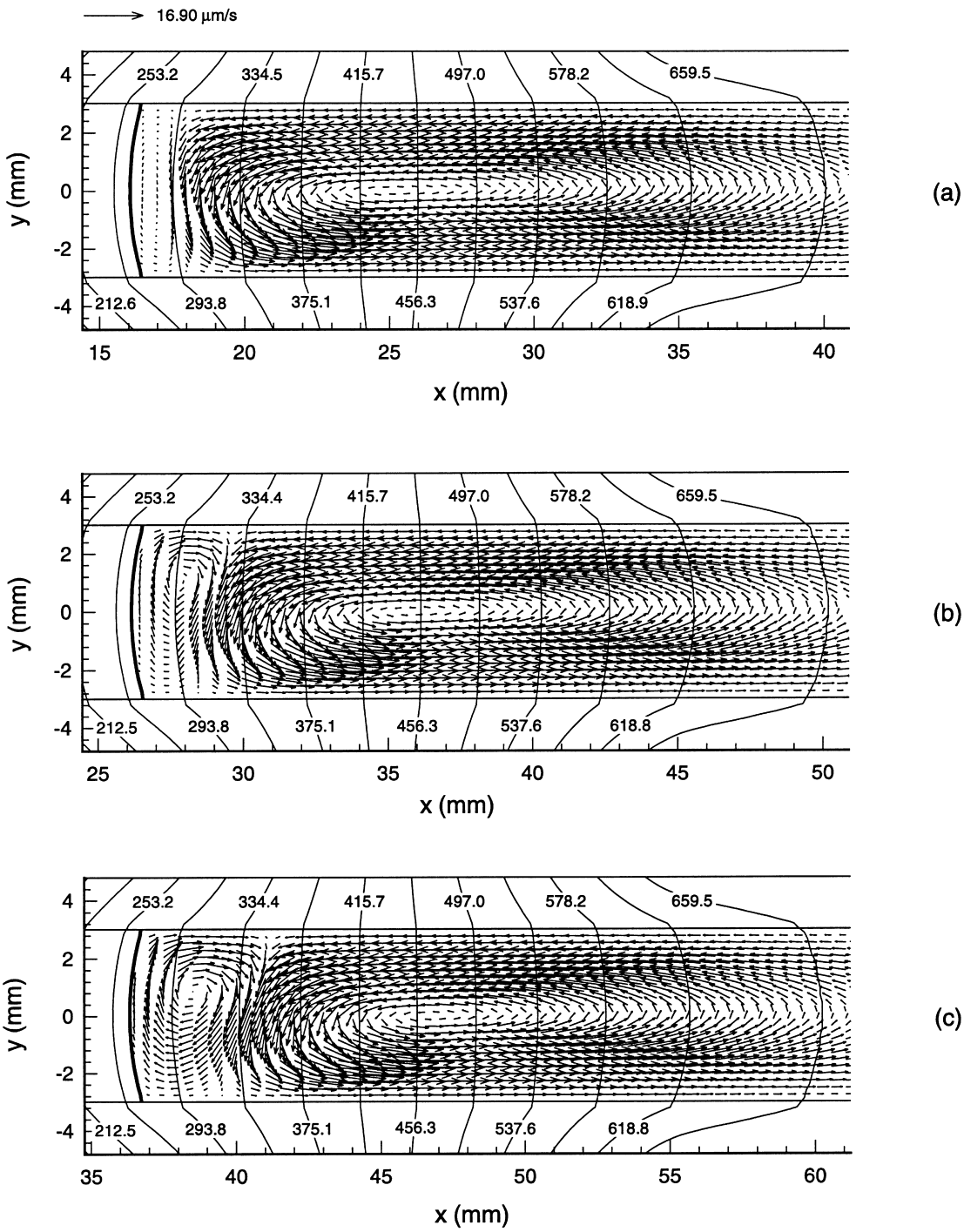

Fig. 9. Velocity vectors and isotherms for horizontal Bridgman growth with $g = 50$ μg at (a) 3000 (b) 6000 and (c) 9000 s. The thick solid line indicates the location of the interface. Note the intensity of the velocities in the secondary cell when compared to those in Fig. 4.

liquid and solid for the g = 50 μg case. The results are dramatically different from those shown in Figs. 6 and 8. The boundary layers no longer exhibit the characteristic exponential profile of diffusion-dominated conditions: a break-down in diffusion-dominated growth has occurred. There are several interesting phenomena that may be observed. At 3000 s the traces are the result of the action of the thermally driven primary convective cell which dominates the convection in the melt up to this time. Convective velocities move towards the interface in the $y > 0$ region and then down and away from the interface in the $y > 0$ region. Correspondingly, the y = 2.88 mm trace exhibits a compact solute boundary layer and has a lower peak value than the $y = -2.88$ mm trace, which has a higher peak value and is much more diffuse (the layer extends to $x \approx 38$ mm!). At later times, the boundary layers are more complicated. The increased strength and size of the secondary convective cell causes much larger peak values for the y = 2.88 mm trace than for the $y = -2.88$ mm trace. Furthermore, solute transported into the secondary cell is entrained into the primary cell and swept out into the bulk, resulting in thicker solute boundary layers in the $y < 0$ portion of the domain. Note that the boundary layer for the trace at $y = -2.88$ mm extends to $x \approx 60$ mm.

Fig. 12 is a plot of *average* solute concentrations in the solid at 3000, 6000 and 9000 s for the 1, 10 and 50 μg cases. Averaging is performed across the height of the solidified material ($y = -3$ to 3 mm). For comparison purposes, average concentrations for the pure diffusion case as well as those calculated from an exact analytical expression for solid solute concentrations under 1D, pure diffusion growth conditions [20] are also shown. The pure diffusion results exhibit good agreement with the 1D analytical result; the largest difference between these results is 1.7% at 9000 s. The results for the 1 μg case are not significantly different from the diffusion-only case results. This indicates that at this gravity level, the process remains diffusion-controlled. The average solute concentrations for the g = 10 μg case are discernibly lower than for the 1 μg case,

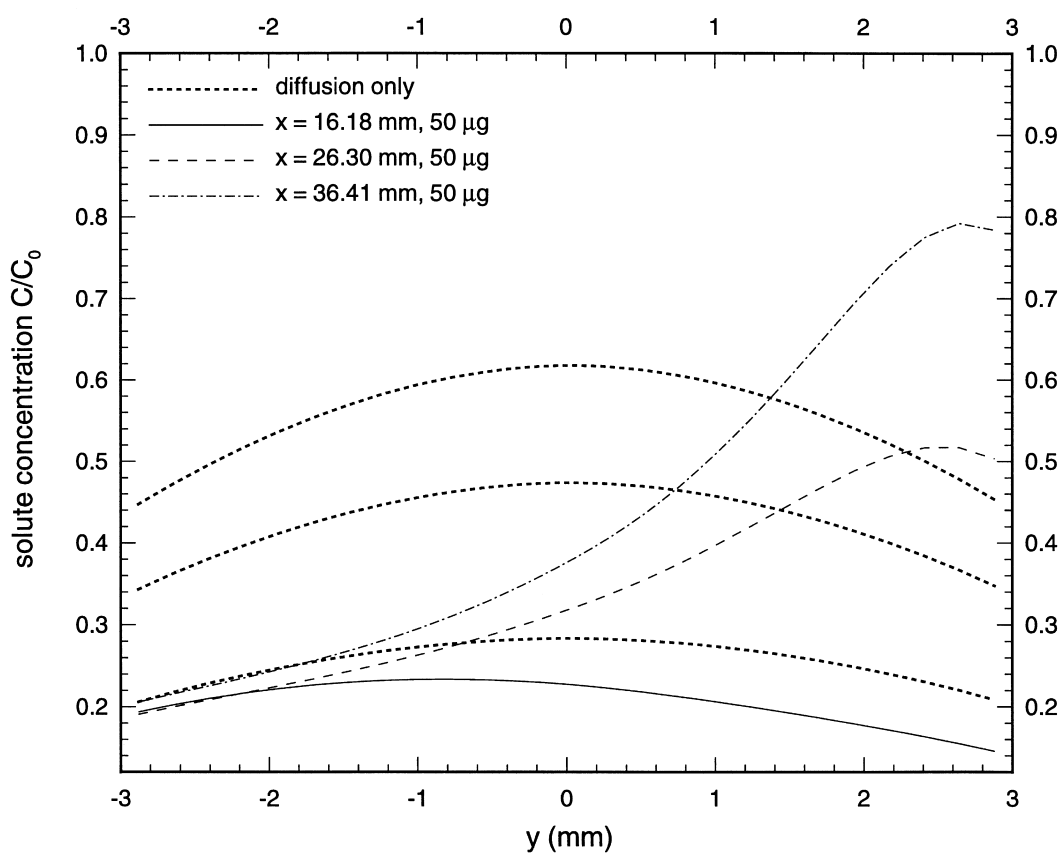

Fig. 10. Traces of solute concentration across the solidified material at various x-locations for g = 50 μg. The dotted lines correspond to diffusion-only (no convection) results.

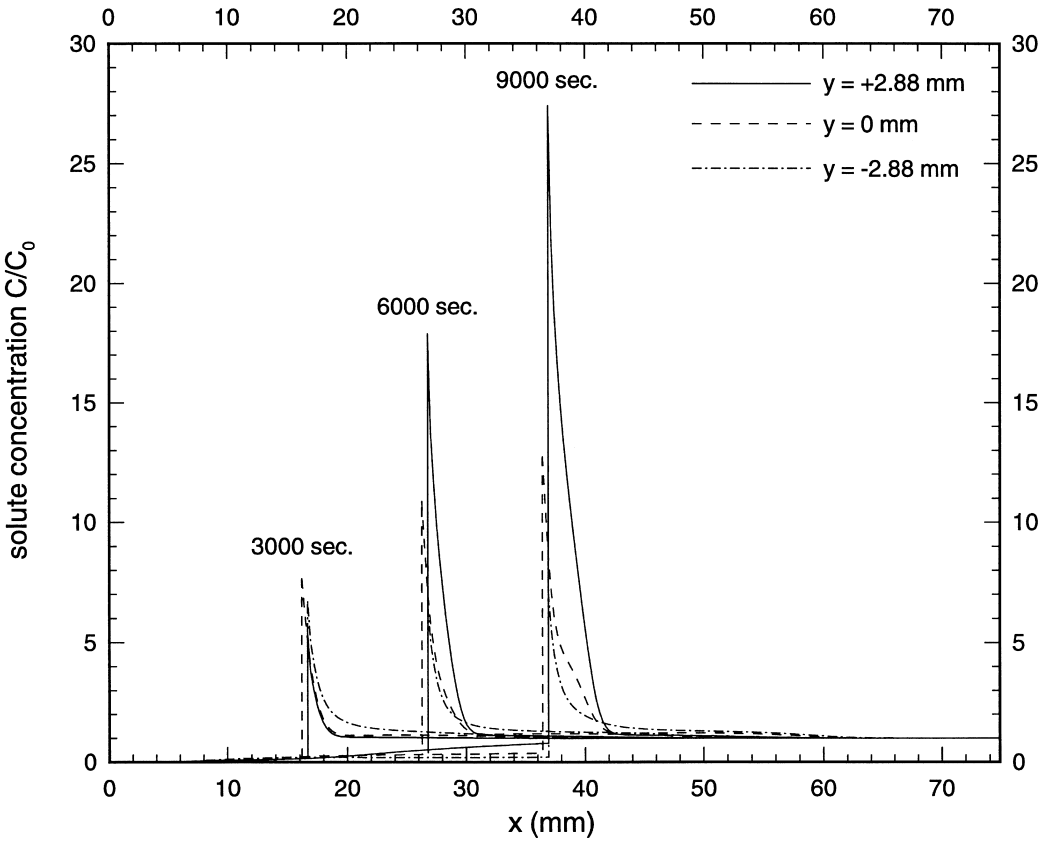

Fig. 11. Longitudinal solute concentration traces at three different y-locations for $g = 50$ μg.

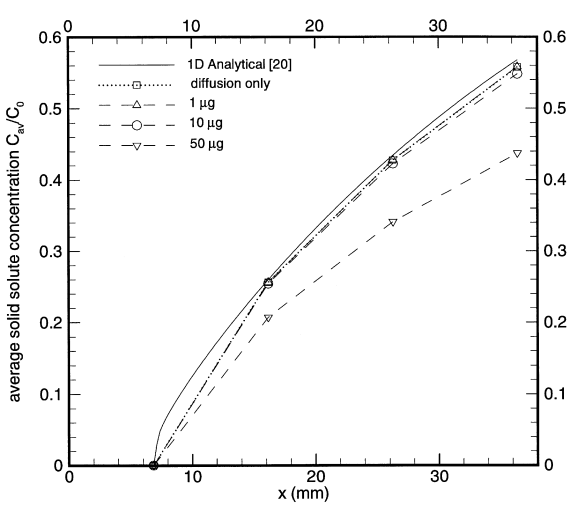

Fig. 12. Comparison of average concentration values in the solidified material. The solid line is the 1D analytical result [20]. The result for $g = 50$ μg is significantly different from the pure-diffusion result, indicating a breakdown to convective-controlled conditions.

registering 0.8, 1.1 and 1.7% lower values than for the pure diffusion case after 3000, 6000 and 9000 s, respectively. This indicates that some solute is being swept away from the near-interface region by the slightly higher levels of convection; the results have deviated from diffusion-controlled conditions. For the $g = 50$ μg case, the average values are significantly lower than those found in the other cases. The larger values of convection, in general, act to sweep solute away from the interface and into the bulk (refer to Figs. 9–11) and thus lower the average value of solute concentration forming in the solid.

5. Conclusions

A series of fully transient simulations of horizontal Bridgman crystal growth at various gravity levels have been performed. The binary alloy being considered is Bi-1.0 at.% Sn. The results from these simulations have elucidated the influence of thermosolutal convec-

tion on longitudinal and radial solute profiles during the process.

As time proceeds and the crystal solidifies, solute is rejected at the interface and the level of solute near the interface increases, leading to the formation of a solute boundary layer. Initially, a single, thermally driven, counter-clockwise rotating cell is present. As solute accumulates at the interface, a secondary, solute-driven clockwise rotating cell develops. For a gravity level of $g = 1$ μg, the magnitudes of the velocities in the domain are small; the solute boundary layers are not significantly altered from the pure diffusion case. Radial segregation due to convection is also slight. For $g = 10$ μg, the magnitudes of the velocities in the melt are larger. The effect of these increased convective levels is to perturb the solute boundary layers from their ideal diffusion-only profiles and yield significant levels of segregation in the solute at the interface (and hence in the solid). This segregation is such that the values toward the top of the domain are highest. For the highest gravity level of $g = 50$ μg, the solute redistribution process has completely departed from being diffusion-controlled; convection plays a very significant role in the process. The solute boundary layers are dramatically different from the diffusion-controlled profiles as a result of the complex convection pattern in the melt. Very large levels of radial segregation are observed in the solidified material, due to the transport of solute to the y > 0 portion of the domain under the action of convection.

The values of concentration encountered at the interface (especially at later times) would result in a significant change in the melting temperature of the alloy. Further simulations of Bridgman crystal growth, incorporating the effects of a concentration-dependent melting temperature, are planned as future work.

Acknowledgements

Partial funding for this work from NASA (Coop. Agreement ♯NCC3-557) is gratefully acknowledged. JES was funded by a UW-Milwaukee Graduate School Fellowship. The insightful help of Henry de Groh III of NASA-Glenn is much appreciated. Professors G. de Vahl Davis and E. Leonardi and Dr V. Timchenko of the University of New South Wales are thanked for kindly providing their code, FRECON3V, which formed the basis for the velocity solver in this work.

Appendix A. Discrete form of energy equation

The energy equation, Eq. (1), is discretized using the finite volume mesh (Fig. 2). An upwind scheme is incorporated for the treatment of convective heat fluxes. This discretization may then be written as

$$
\begin{aligned}
&A_{i,j}^{n+1}\frac{T_{i,j}^{n+1}-T_{i,j}^{n}}{\Delta t}\Delta x\Delta y \\
&\quad=\rho c_{\mathrm{pL}}\Delta y[T_{i,j}^{n+1}[\![u_{i-1/2,j},0]\!]-T_{i-1,j}^{n+1}[\![-u_{i-1/2,j},0]\!] \\
&\quad+T_{i,j}^{n+1}[\![-u_{i+1/2,j},0]\!]-T_{i+1,j}^{n+1}[\![u_{i+1/2,j},0]\!]] \\
&\quad+\rho c_{\mathrm{pL}}\Delta x[T_{i,j}^{n+1}[\![v_{i,j-1/2},0]\!]-T_{i,j-1}^{n+1}[\![-v_{i,j-1/2},0]\!] \\
&\quad+T_{i,j}^{n-1}[\![-v_{i,j+1/2},0]\!]-T_{i,j+1}^{n+1}[\![v_{i,j+1/2},0]\!]] \\
&\quad+\Delta y[k_{i+1/2,j}(T_{i+1,j}^{n+1}-T_{i,j}^{n+1})/\Delta x-k_{i-1/2,j}(T_{i,j}^{n+1} \\
&\quad-T_{i-1,j}^{n+1})/\Delta x]+\Delta x[k_{i,j+1/2}(T_{i,j+1}^{n+1}-T_{i,j}^{n+1})/\Delta y \\
&\quad-k_{i,j-1/2}(T_{i,j}^{n+1}-T_{i,j-1}^{n+1})/\Delta y]
\end{aligned}
$$

in which $[\![X, Y]\!]$ is the maximum of X and Y. The discrete form of the apparent heat capacity A (Eq. (3)) is

$$
\begin{aligned}
A_{i,j}^{n+1}&=\rho(c_{\mathrm{pL}}f_{\mathrm{L}}^{n+1}+c_{\mathrm{pS}}f_{\mathrm{S}}^{n+1})+\rho[(c_{\mathrm{pL}}-c_{\mathrm{pS}})T^{n+1} \\
&\quad+h_0]\left(\frac{\partial f_{\mathrm{L}}}{\partial T}\right)^{n+1}.
\end{aligned}
$$

Appendix B. Discrete form of concentration equation

The discretized analog of Eq. (4) using the finite volume mesh and upwinding for the convective terms is

$$
\begin{aligned}
&\frac{C_{\mathrm{L}i,j}^{n+1}-C_{\mathrm{L}i,j}^{n}}{\Delta t}\Delta x\Delta y \\
&\quad=\Delta y[C_{\mathrm{L}i,j}^{n+1}[\![u_{i-1/2,j},0]\!]-C_{\mathrm{L}i-1,j}^{n+1}[\![-u_{1-1/2,j},0]\!] \\
&\quad+C_{\mathrm{L}i,j}^{n+1}[\![-u_{i+1/2,j},0]\!]-C_{\mathrm{L}i+1,j}^{n+1}[\![u_{i+1/2,j},0]\!]] \\
&\quad+\Delta x[C_{\mathrm{L}i,j}^{n+1}[\![u_{i,j-1/2},0]\!]-C_{\mathrm{L}i,j-1}^{n+1}[\![-u_{i,j-1/2},0]\!] \\
&\quad+C_{\mathrm{L}i,j}^{n+1}[\![-u_{i,j+1/2},0]\!]-C_{\mathrm{L}i,j+1}^{n+1}[\![u_{i,j+1/2},0]\!]] \\
&\quad+\Delta y\left[D_{i+1/2,j}\frac{C_{\mathrm{L}i+1,j}^{n+1}-C_{\mathrm{L}i,j}^{n+1}}{\Delta x}\right. \\
&\quad\left.-D_{i-1/2,j}\frac{C_{\mathrm{L}i,j}^{n+1}-C_{\mathrm{L}i-1,j}^{n+1}}{\Delta x}\right] \\
&\quad+\Delta x\left[D_{i,j+1/2}\frac{C_{\mathrm{L}i,j+1}^{n+1}-C_{\mathrm{L}i,j}^{n+1}}{\Delta y}\right. \\
&\quad\left.-D_{i,j-1/2}\frac{C_{\mathrm{L}i,j}^{n+1}-C_{\mathrm{L}i,j-1}^{n+1}}{\Delta y}\right]+S_{i,j}
\end{aligned}
$$

in which $[\![X, Y]\!]$ is the maximum of X and Y. The discrete form of source term S (Eq. (6)) becomes

$$S_{i,j} = C^{n+1}_{\mathrm{L}i,j}\frac{(1-k_{\mathrm{p}})(f^{n}_{\mathrm{L}} - f^{n+1}_{\mathrm{L}})}{\Delta t}\Delta x\Delta y + \frac{(1-f^{n+1}_{\mathrm{L}})(C^{n+1}_{\mathrm{L}i,j} - C^{n}_{\mathrm{L}i,j})}{\Delta t}\Delta x\Delta y.$$

References

[1] W. Kurz, D.J. Fisher, Fundamentals of Solidification, Trans Tech Publications, 1989.

[2] J.I.D. Alexander, J. Ouazzani, F. Rosenberger, Analysis of the low gravity tolerance of Bridgman–Stockbarger crystal growth, J. Crystal Growth 97 (1989) 285–302.

[3] M. Yao, R. Raman, H.C. de Groh III, Numerical simulation of heat and mass transport during space crystal growth with MEPHISTO, NASA Technical Memorandum 107015, 1995.

[4] P.M. Adornato, R.A. Brown, Convection and segregation in directional solidification of dilute and non-dilute binary alloys, J. Crystal Growth 80 (1987) 155–190.

[5] M.C. Liang, C.W. Lan, Three-dimensional convection and solute segregation in vertical Bridgman crystal growth, J. Crystal Growth 167 (1996) 320–332.

[6] M. Yao, H.C. de Groh III, R. Abbaschian, Numerical modeling of solidification in space with MEPHISTO-4 (Part 1), in: Proceedings of 35th Aerospace Sciences Meeting and Exhibit, Reno, NV, 1997 Paper AIAA 97-0449.

[7] H.C. de Groh III, E.S. Nelson, On residual acceleration during space experiments, Heat Transfer in Microgravity Systems ASME HTD 290 (1994) 23–33.

[8] J.E. Simpson, S.V. Garimella, H.C. de Groh III, R. Abbaschian, Numerical simulations of crystal growth of an alloy under microgravity conditions, in: Proceedings of ASME National Heat Transfer Conference, Albuquerque, New Mexico, ASME NHTC99-204, 1999, pp. 1–9.

[9] V. Timchenko, P.Y.P. Chen, Davis G. de Vahl, E. Leonardi, Directional solidification in microgravity, Heat Transfer 7 (1998) 241–246.

[10] J.E. Simpson, S.V. Garimella, Melt convection and front propagation in the unidirectional solidification of a pure material, in: J. Beech, H. Jones (Eds.), Proceedings of Fourth Decennial International Conference on Solidification Processing, Sheffield, UK, 1997, pp. 130–134.

[11] J.E. Simpson, S.V. Garimella, An investigation of the solutal, thermal and flow fields in unidirectional alloy solidification, Int. J. Heat Mass Transfer 41 (1998) 2485–2502.

[12] X. Zeng, A. Faghri, Temperature-transforming model for binary solid–liquid phase-change problems — part 1: mathematical modeling and numerical methodology, Num. Heat Transfer B 25 (1994) 467–480.

[13] J.A. Dantzig, Modelling liquid–solid phase changes with melt convection, Int. J. Num. Methods Engineering 28 (1989) 1769–1785.

[14] V.R. Voller, A.D. Brent, C. Prakash, The modelling of heat, mass and solute transport in solidification systems, Int. J. Heat Mass Transfer 32 (1989) 1719–1731.

[15] C.R. Swaminathan, V.R. Voller, Towards a general numerical scheme for solidification systems, Int. J. Heat Mass Transfer 30 (1997) 2859–2868.

[16] R. Barrett, M. Berry, T.F. Chan, J. Demmel, J.M. Donato, J. Dongarra, V. Eijkhout, R. Pozo, C. Romine, H. Van der Vorst, Templates for the Solution of Linear Systems: Building Blocks for Iterative Methods, SIAM, Philadelphia, 1994.

[17] S.V. Garimella, J.E. Simpson, Interface propagation in the processing of metal matrix composites, Microscale Thermophysical Engineering 2 (1998) 173–188.

[18] J.E. Simpson, S.V. Garimella, H.C. de Groh III, R. Abbaschian Melt convection effects in the Bridgman crystal growth of an alloy under microgravity conditions. In: Proceedings of Seventh AIAA/ASME Joint Thermophysics and Heat Transfer Conference ASME HTD, 1998. 357-4, pp. 123–132.

[19] S.R. Coriell, R.F. Sekerka, Lateral solute segregation during unidirectional solidification of a binary alloy with a curved solid–liquid interface, J. Crystal Growth 46 (1979) 479–482.

[20] V.G. Smith, W.A. Tiller, J.W. Rutter, A mathematical analysis of solute redistribution during solidification, Canadian J. Phys 33 (1955) 723–743.